POLITECNICO DI TORINO
Repository ISTITUZIONALE

Shape Sensing for an UAV Composite Half-Wing: Numerical Comparison between Modal Method and Ko's Displacement Theory

Original
Shape Sensing for an UAV Composite Half-Wing: Numerical Comparison between Modal Method and Ko's Displacement Theory / Valoriani, Filippo; Esposito, Marco; Gherlone, Marco. - In: AEROSPACE. - ISSN 2226-4310. - ELETTRONICO. - 9:9(2022), p. 509. [10.3390/aerospace9090509]

Availability:
This version is available at: 11583/2971488 since: 2022-11-09T10:24:17Z

Publisher:
MDPI

Published
DOI:10.3390/aerospace9090509

Terms of use:
openAccess

This article is made available under terms and conditions as specified in the corresponding bibliographic description in the repository

Publisher copyright

(Article begins on next page)

29 November 2022

aerospace

MDPI

Article

Shape Sensing for an UAV Composite Half-Wing: Numerical Comparison between Modal Method and Ko's Displacement Theory

Filippo Valoriani *, Marco Esposito and Marco Gherlone

Department of Mechanical and Aerospace Engineering, Politecnico di Torino, 10129 Turin, Italy
* Correspondence: filippo.valoriani@studenti.polito.it

Abstract: Shape sensing is the reconstruction of the displacement field of a structure from some discrete surface strain measurements and is a key technology for structural health monitoring. The aim of this paper is to compare two approaches to shape sensing that have been shown to be more efficient, especially for aircraft structures applications, in terms of required input strain measurements: the Ko's Displacement Theory and the Modal Method. An object of the shape-sensing analysis is the half-wing of a multirotor UAV. The approaches are summarized in order to set the framework for the numerical comparative investigation. Then, the multirotor UAV is presented and a finite element model of its half-wing is used to simulate the static response to straight-and-level flight conditions. For a given common set of surface strain measurement points, Ko's Displacement Theory and the Modal Method are compared in terms of accuracy of the reconstructed half-wing deflection and twist angle. The Modal Method is shown to be more accurate than Ko's Displacement Theory, especially for the evaluation of the deflection field. Further numerical analyses show that the Modal Method is influenced by the set of mode shapes included in the analysis and that excellent reconstructed deflections can be obtained with a reduced number of sensors, thus assessing the approach as an efficient shape-sensing tool for aircraft structures real applications.

Keywords: shape sensing; UAV; strains; Ko's Displacement Theory; Modal Method

check for updates

Citation: Valoriani, F.; Esposito, M.; Gherlone, M. Shape Sensing for an UAV Composite Half-Wing: Numerical Comparison between Modal Method and Ko's Displacement Theory. *Aerospace* **2022**, *9*, 509. https://doi.org/10.3390/aerospace9090509

Academic Editor: Javaan Chahl

Received: 9 August 2022
Accepted: 9 September 2022
Published: 13 September 2022

Publisher's Note: MDPI stays neutral with regard to jurisdictional claims in published maps and institutional affiliations.

Copyright: © 2022 by the authors. Licensee MDPI, Basel, Switzerland. This article is an open access article distributed under the terms and conditions of the Creative Commons Attribution (CC BY) license (https://creativecommons.org/licenses/by/4.0/).

1. Introduction

Shape sensing is the reconstruction of the displacement field of a structure from discrete strain measurements [1] and can play a crucial role in monitoring the health of load-carrying structural components, especially composite multilayered ones that are more prone to damage. Damage-tolerant designs are, in fact, strongly influenced by the possibility of detecting the presence of non-visible damages. A method capable of indirectly monitoring these critical conditions through the evaluation of other quantities, like the displacement field, could bring significant benefits (more accurate determination of maintenance-inspection cycles and identification of critical areas of a structure). Furthermore, real-time evaluation of the displacement field is important in smart structures to implement a feed-back control system for morphing mechanisms [2].

Recent improvements in the strain sensing technology are also facilitating the progress of shape sensing methods based on discrete strain measurements. The development of fiber optic strain sensing systems gives the opportunity to have a multiplex, highly sensible and highly integrated sensor for strain measurement, especially for composite structures. In fact, fiber optic systems based on Fiber Bragg Gratings (FBGs) and, more recently, distributed systems based on Rayleigh scattering and Optical Frequency Domain Reflectometry (OFDR), can be embedded in composite laminates during the layup phase [3,4].

Four main categories of shape sensing methods based on discrete strain measurements have been proposed (refer to [1] for a more complete review and discussion):

1. methods based on numerical integration of experimental strains, in particular the Ko's Displacement Theory ("Ko") [5,6].
2. methods using global or piece-wise linear continuous basis functions to approximate the displacement field, in particular the Modal Method ("MM") [7,8].
3. inverse Finite Element Method ("iFEM"), based on a finite-element discretization and on a variational principle [1,9–11].
4. methods based on the use of the Artificial Neural Networks ("ANNs") [12,13].

The accuracy of methods based on ANNs is heavily biased by the choice of the training load cases [12,13], therefore these approaches have found limited application. Esposito and Gherlone, in [14,15], compared and assessed the other three main methods when applied to the shape sensing of a composite wing box undergoing bending and torsion. iFEM was showed to be the more accurate approach but at the cost of a large number of strain sensors. On the other hand, the Modal Method and Ko's Displacement Theory, although exhibiting a reduced accuracy, were able to efficiently work with a limited number of local strain measurements.

The Displacement Theory of Ko, Tran, and Richards [5,16] is based on the classical Bernoulli–Euler beam theory. Through axial strain measurements at discrete positions along a line, it is possible to evaluate the curvature. Double integration of the curvature provides the deflection shape at the same discrete locations. Using more than one sensing line along the span of a wing structure, it is also possible to evaluate the cross-sectional twist angle due to torsion. The Ko's Displacement Theory was applied to the deformed shape analysis of the wing of the Ikhana UAV. Two measurement lines were set along the wingspan to rebuild the deflections and cross-sectional twist, then the data were compared with those computed from a finite element model [16]. Jutte et al. [17] performed a ground test of a full-scale wing using a fiber optic strain-sensing system. After reconstructing the bending and twist deformation of the wing through the Ko's Displacement Theory, the results were compared with the experimental ones obtained with a photogrammetric approach, and a very good degree of accuracy was obtained.

The Modal Method, developed by Foss and Haugse [8] and Pisoni, Santolini, Hauf, and Dubowsky [18] in 1995, can reconstruct the displacement field of any structure using its mode shapes and some strain measurements at discrete locations. The displacement and strain fields are expressed in terms of known shape functions (the mode shapes and the spatial derivatives of the mode shapes, respectively) and unknown weights (the modal coordinates). The modal coordinates are computed by fitting the reconstructed strain field on to the measured one at discrete locations. The knowledge of the modal coordinates allows the reconstruction of the displacement field. The work by Bogert, Haugse, and Gehrki [7] also included a criterion for selecting the most suitable mode shapes for the application of the method. The selection criterion is based on the evaluation of the strain energy contribution of each mode shape. Rapp et al. [19] examined in depth the influence of the number and location of the strain sensors on the accuracy of the method, highlighting the importance of sensors' positioning, especially when using a small number of discrete strain measurements.

The aim of the current effort is to investigate the shape sensing of an UAV composite wing by means of the approaches that, in their current formulation, require a limited (and practically affordable) number of strain sensors: the Modal Method and Ko's Displacement Theory. The paper is organized as follows. At first, the two approaches are briefly introduced in order to set the numerical framework for the analysis. Then, the UAV wing structure is described and its finite element model is built as a source for both the input strain measurements and the reference displacement field. Both shape-sensing methods are then applied and the reconstructed deformed shapes assessed trough comparison with the reference displacement field.

2. Summary of the Shape-Sensing Methods

In this section, the basic equations of the Ko's Displacement Theory and of the Modal Method are provided.

2.1. Ko's Displacement Theory

Ko's Displacement Theory exploits the Bernoulli–Euler beam theory to compute the deflection of a beam-like structure along a line where axial strains are measured [5]. Considering the clamped structure in Figure 1, the marked line along the s coordinate represents the path along which strain ε_{ss} are measured. There are $(N + 1)$ locations where strains are measured, s_i $(i = 0, 1, \ldots, N)$, with s_0 and s_N denoting the coordinates at the clamped end and at the tip of the beam, respectively. Therefore, the measured strains are denoted by $\varepsilon_i \equiv \varepsilon_{ss}(s_i)$. Following the assumptions of the Euler–Bernoulli theory for pure bending, it is possible to express the longitudinal strains in terms of the second derivatives of the deflection $(w_{,ss})$ [5]

$$\varepsilon_{ss}(s) = -\mathrm{c}w_{,ss}(s) \tag{1}$$

where c is the distance between the sensor and the neutral axis of the beam. Isolating for $w_{,ss}(s)$, we have

$$w_{,ss}(s) = -\frac{\varepsilon_{ss}(s)}{c} \tag{2}$$

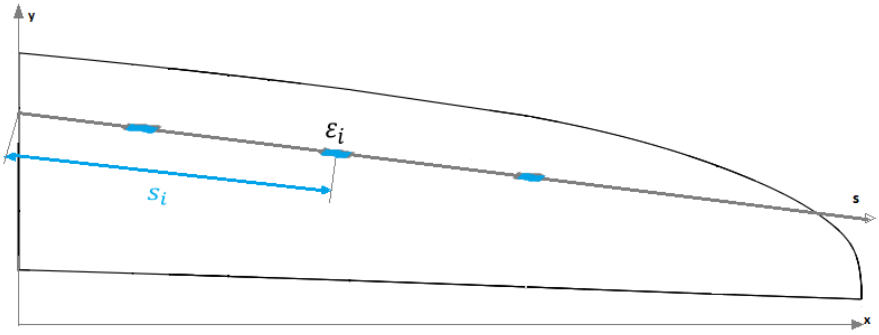

Figure 1. Half-wing with reference system and sensor markers.

The subscript ss will be omitted in the rest of the discussion, assuming that ε will always be along the direction of the measurement line. The longitudinal strains are measured in $(N + 1)$ discrete positions and they are assumed to change linearly between one measurement station and the next one. In a variable-cross-section beam (for example, in a tapered wing), $c = c(s)$, and the assumption is made that it is a linear function of the coordinate s between the measurement locations [5].

$$\begin{aligned} \varepsilon(s) &= \varepsilon_{i-1} - (\varepsilon_{i-1} - \varepsilon_i)\tfrac{s-s_{i-1}}{s_i-s_{i-1}} \\ c(s) &= c_{i-1} - (c_{i-1} - c_i)\tfrac{s-s_{i-1}}{s_i-s_{i-1}} \\ s_{i-1} &< s < s_i (i = 1, 2, \ldots, N) \end{aligned} \tag{3}$$

For practical reasons, it is difficult to measure the strain value at the tip and at the clamped end. However, this problem can be overcome by setting the strain at the wing tip as $\varepsilon_n = 0$ and, for the strain at the clamp, by obtaining ε_0 through extrapolation from the near strain measurements.

The transverse deflection at the strain-measurement points, $w_i \equiv w(s_i)$, $(i = 1, 2, \ldots, N)$, can be obtained by double integrating Equation (2), considering appropriate boundary conditions ($w(s = 0) = 0$ and $w_{,s}(s = 0) = 0$) and the continuity of deflections (w) and cross-section rotations $(w_{,s})$ at each strain measurement point [5].

By adopting an arrangement with two parallel sensor lines (distance d), it is possible to evaluate the twist angle β generated by torsion by considering the deflections along one line (w_i) and deflections along the other line (w_i') [5].

$$\beta_i = \sin^{-1}\left(\frac{w_i - w_i'}{d}\right)(i = 1,\ 2,\ \ldots, N) \tag{4}$$

2.2. Modal Method

The Modal Method is based on a modal transformation since it can reconstruct the displacement field of any structure using its mode shapes and some discrete strain measurements [8]. Assuming that a finite element discretization of the structure has been introduced, the displacement and strain fields are expressed as a function of the modal coordinates q [8]:

$$\boldsymbol{w} = \boldsymbol{\phi}_d\, q \tag{5}$$

$$\boldsymbol{\varepsilon} = \boldsymbol{\phi}_s\, q \tag{6}$$

where $\boldsymbol{w}$ is the vector contains the displacements degrees of freedom, $\boldsymbol{\varepsilon}$ is the vector of discrete strains, and $\boldsymbol{\phi}_d$ and $\boldsymbol{\phi}_s$ are the modal matrices corresponding, respectively, to displacements and strains (each column represents the displacement or strain vector associated to the corresponding mode shape). Displacement mode shapes and strain mode shapes can be easily computed through a finite element analysis, but they could be significantly difficult to estimate experimentally [8]. From Equation (6) it is possible to express modal coordinates as function of the strains

$$\boldsymbol{q} = \boldsymbol{\phi}_s^{-1}\boldsymbol{\varepsilon} \tag{7}$$

Then, replacing Equation (7) in Equation (5), we obtain

$$\boldsymbol{w} = \boldsymbol{\phi}_d\boldsymbol{\phi}_s^{-1}\boldsymbol{\varepsilon} \tag{8}$$

This allows us to obtain the displacement degrees of freedom as functions of the modal matrices and of the strain vector. As in real situations it is unlikely that the number of available strains (S) is equal to the number of calculated mode shapes (M), the method has to deal with non-square $\boldsymbol{\phi}_d$ matrices. This problem can be overcome using a least-square approach via the Moore–Penrose pseudo-inverse matrix formulation, thus obtaining a more general form of Equation (7) and of Equation (8) [8].

$$\boldsymbol{q} = \left(\boldsymbol{\phi}_s^T\boldsymbol{\phi}_s\right)^{-1}\boldsymbol{\phi}_s^T\boldsymbol{\varepsilon} \tag{9}$$

$$\boldsymbol{w} = \boldsymbol{\phi}_d\left(\boldsymbol{\phi}_s^T\boldsymbol{\phi}_s\right)^{-1}\boldsymbol{\phi}_s^T\boldsymbol{\varepsilon} \tag{10}$$

When $S < M$, the problem admits an infinite number of solutions, whereas, for $S > M$, the number of equations exceeds the number of unknowns, and the problem can be solved by using Equation (10). The condition that requires the number of available strains to be higher than the number of mode shapes used in the displacements and strains approximation leads to the need for a mode selection criterion. Bogert, Haugse, and Gehrki have proposed an approach to select a reduced number of mode shapes that contribute to representing the static deformation of the structure [7]. Once a reduced number of modes (M_r) is selected, the relative modal displacement matrix $\boldsymbol{\phi}_{dr}$ is generated. The so-obtained matrix can be inserted into Equation (5) and, pseudo inverting it, we can obtain the modal coordinates vector relative to the retained modes, $\boldsymbol{q}_r$

$$\boldsymbol{q}_r = \left(\boldsymbol{\phi}_{dr}^T\boldsymbol{\phi}_{dr}\right)^{-1}\boldsymbol{\phi}_{dr}^T\boldsymbol{w} \tag{11}$$

$\boldsymbol{q}_r$ represents the modal coordinate vector that best fit, according to the least squares method, the static deformation described by the displacement's vector, $\boldsymbol{w}$, using only a reduced number of modes. Using the reduced modal coordinates vector, it is possible to compute the approximated modal representation of the static solution, $\boldsymbol{w}_r$, using only the retained modes [7]

$$\boldsymbol{w}_r = \boldsymbol{\phi}_{dr}\boldsymbol{q}_r \tag{12}$$

The modal representation of the static solution can be written as the summation of the contributions of each mode

$$\boldsymbol{w}_r = \sum_{i=1}^{M_r} \boldsymbol{\phi}_{dr_i} q_{r_i} \tag{13}$$

where $\boldsymbol{\phi}_{dr_i}$ is a column of the matrix $\boldsymbol{\phi}_d$ and q_{r_i} is the i-th modal coordinate. The contribution of the i-th mode the displacement vector is

$$\boldsymbol{w}_{r_i} = \boldsymbol{\phi}_{dr_i} q_{r_i} \tag{14}$$

From this contribution, it is possible to compute the strain energy associated with each i-th mode [7]

$$E_{r_i} = \frac{1}{2}\boldsymbol{w}_{r_i}^T \boldsymbol{K}\, \boldsymbol{w}_{r_i} \tag{15}$$

where $\boldsymbol{K}$ is the stiffness matrix. Replacing Equation (14) into Equation (15)

$$E_{r_i} = \frac{1}{2} q_{r_i}^T \boldsymbol{\phi}_{dr_i}^T \boldsymbol{K}\, \boldsymbol{\phi}_{dr_i} q_{r_i} \tag{16}$$

Considering mode shapes normalized with respect to the mass matrix, we have that:

$$\boldsymbol{\phi}_{dr_i}^T \boldsymbol{K}\, \boldsymbol{\phi}_{dr_i} = \omega_i^2 \tag{17}$$

where ω_i^2 is the angular frequency associated to the i-th mode. Therefore, Equation (16) can be re-written as

$$E_{r_i} = \frac{1}{2}\omega_i^2 q_{r_i}^2 \tag{18}$$

This formulation allows the computation of the elastic strain energy of each mode. By comparing it with the total elastic strain energy corresponding to the static deformation, it is possible to evaluate the contribution of each mode to the total elastic strain energy. As a consequence, the capability of each mode to represent the static deformation can be derived evaluating this contribution. All this leads to the formulation of a selection criterion for the modes, based on the strain energy.

In the context of the modes' selection, it is important to consider that only a subset of the mode shapes of a structure is computed during a modal analysis. Although the computed modes may be able to represent the static deformation of the structure, sometimes the omission of higher-frequency modes can lead to significant loss in the accuracy of the Modal Method. In fact, higher-frequency modes can help to improve the representation of the structure's static deformation. To reduce the lack of information due to the omission of the high-frequency modes, the effect of including the residual vectors within the retained modes is explored in this work. The residual vectors are mode shapes based on the static response of the structure to given loads [20]. They can be computed using FE commercial codes. In the present investigation, the residual vectors computed by MSC NASTRAN and based on the formulation introduced by Rose in 1991 [21], Dickens in 2000 [22], and reported by Wijker in [23], are considered.

3. Multirotor UAV

In this section, we describe the ICON V2 UAV and its half-wing, object of the present shape-sensing comparative study, and we provide details on the finite element model that has been used to simulate the static response of the structure.

3.1. Geometry and Material Properties

ICON V2 is a multirotor (Figure 2) provided by the company PROS3 [24]. ICON V2 is able to take off at a fixed point, as a tilt-rotor aircraft, by using 4 propellers mounted on the support arms. During the cruise phase, the aircraft is pushed by a propeller mounted on the back of the fuselage, while the other 4 are disabled. The UAV is designed to be able to perform both aero-photogrammetry and search and rescue missions. The fuselage, the wing, the tail, and the support arms that connect the wing to the tail are made of composite materials (both glass fiber reinforced polymers—GFRP—and carbon fiber reinforced polymers—CFRP). Table 1 reports the main properties of the UAV.

(**a**)

(**b**)

Figure 2. Multirotor ICON V2, PROS3. (**a**) Back view of the aircraft, not operative at ground, (**b**) front view of the UAV during take-off, the rear propeller is switched off during this phase.

Table 1. Main features of ICON V2.

ICON V2	
Wingspan	2.4 m
Length	0.9 m
MTOW	12 kg
Engines	5, brushless

In Figure 3, a disassembled half-wing of the aircraft is shown. Figure 3 summarizes the dimensions of the structure. The wing also has two CFRP tubular spars that cross the fuselage, connecting the two half-wings.

The half-wing structure is made up of multilayered parts (CFRP, GFRP, and balsa) and of a foam that allows the connection of the tubular spars with the panels (Table 2). The adopted composite materials mechanical properties are confidential and the multilayered parts lay-ups are confidential as well. Therefore, standard mechanical properties have been used in the numerical model of the UAV (Table 3). Moreover, all composite and balsa parts are assumed to consist of 10 layers with the stacking sequence [0/45/–45/90/0]°s. For spars and panels, the 0°-direction is aligned with the wing-span direction, whereas, for the ribs, the 0°-direction is aligned with the rib major dimension.

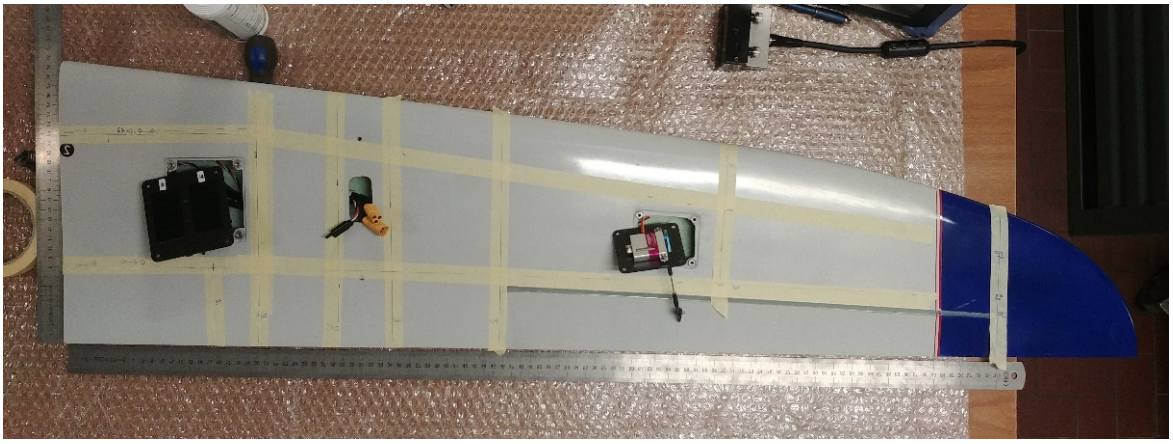

(**a**)

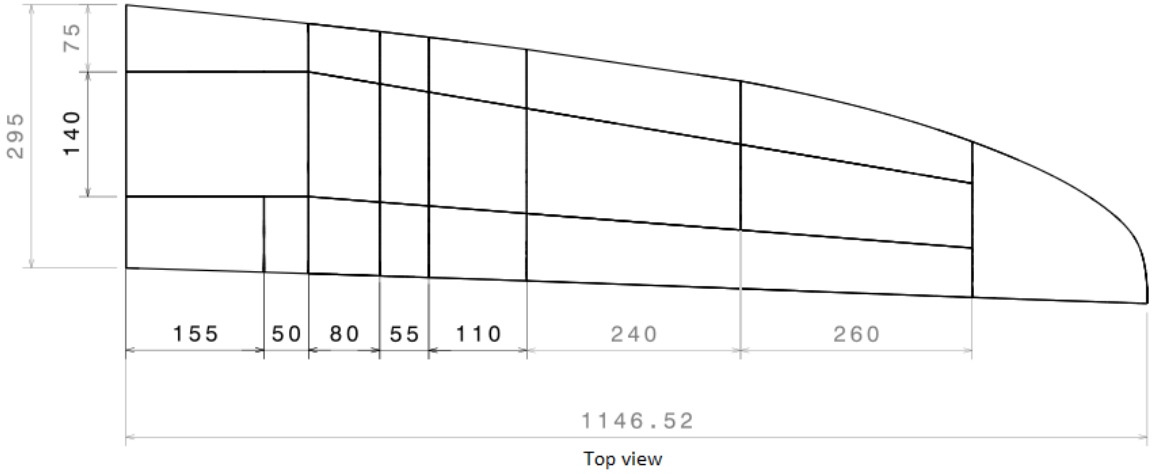

(**b**)

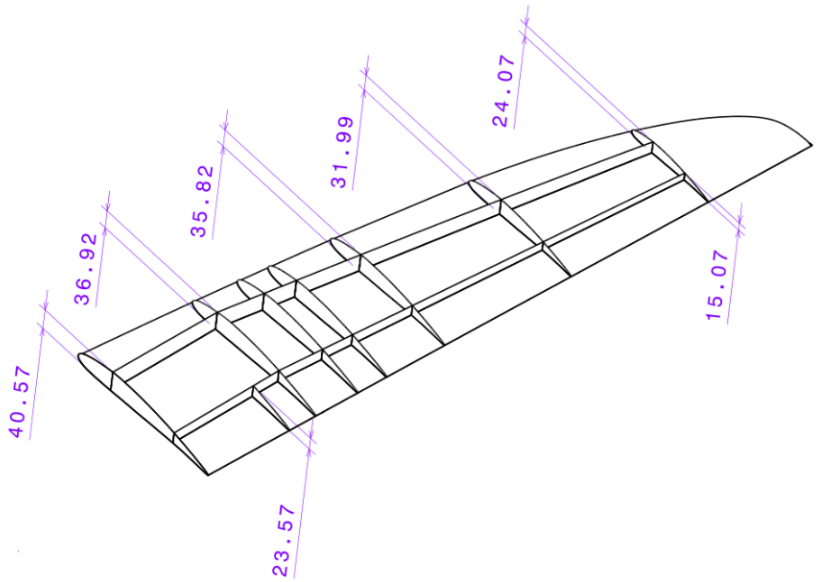

(**c**)

Figure 3. *Cont.*

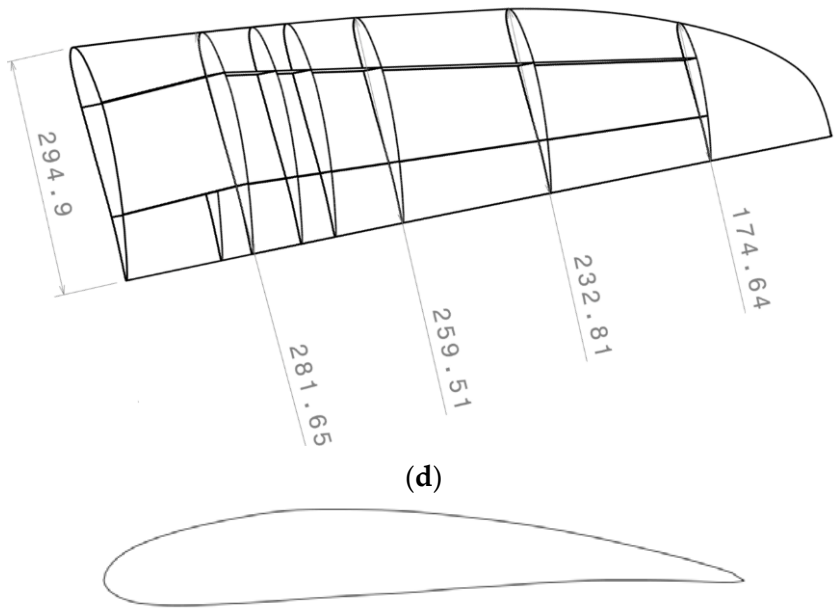

(**d**)

(**e**)

Figure 3. Geometry of the half-wing, dimensions reported in millimeters. (**a**) ICON V2 disassembled half-wing (tape is attached on the external surface as a guide to indicate the position of ribs and spars), (**b**) drafting with quotations, TOP view, (**c**) axonometry with quotations, ribs height, (**d**) axonometry with quotations, ribs length, (**e**) wing airfoil (for confidentiality reasons, the airfoil type is not specified and its geometry has been directly taken from the CAD model provided by the PROS3 company).

Table 2. Material and thickness of the sub-components of the half-wing.

Part	Material	Thickness [mm]
Upper and lower panels	GFRP	1.6
Ribs	Balsa	3
Spars	Balsa	3
Tubular spars	CFRP + foam	1 + 5

3.2. Half-Wing Finite Element Model

In order to perform a shape-sensing analysis of the ICON V2 half-wing with the G's Displacement Theory and the Modal Method, since experimental data are not available, a FE model has been created with MSC/PATRAN. This model should provide: (1) the reference displacement field to assess the accuracy of both shape-sensing methods, (2) the input strains for both approaches, (3) the mode shapes for the Modal Method. Figure 4 shows an overall view of the model. The upper and lower panels are discretized with QUAD4 elements, the ribs, and non-tubular spars with QUAD4 and few TRIA3 elements, and tubular spars with BAR2 and QUAD4 elements (BAR2 elements model the tubular spars, whereas the foam allowing the connection with the upper and lower panels is modelled with QUAD4 elements. Refer to Figure 4). Shell elements have been used for thin-walled components (mainly QUAD4 elements with a few TRIA3 elements where needed to fit sharp corners, as obtained by the automatic mesh utility of MSC/PATRAN). BAR2 elements have been used for the tubular spars (instead of shell elements) since these components do not require a high-fidelity evaluation of strains (no strain sensors are used on the tubular spars). A total of 1615 QUAD4 elements, 86 TRIA3 elements, 19 BAR2 elements, and 1500 nodes have been used. A sensitivity and convergence analysis has been performed, revealing that more refined meshes would improve the accuracy on displacements and strains no more than 1%. In Figure 4b, the rectangular opening on

the trailing edge is actually occupied by the aileron not currently displayed. The aileron has the same characteristics as the upper and lower panels (1.6 mm of GFRP) and is in fact considered part of them. In some figures ahead, it is not displayed for merely graphical reasons.

Table 3. Material properties.

Properties	GFRP	CFRP	Balsa	Foam
E_1 [MPa]	47,712	104,556	1900	36
E_2	12,997	7339	50	
G_{12}	4723	4826	40	14
G_{13}	4723	4826	40	
G_{23}	4723	4826	40	
Poisson ratio [-]	0.115	0.335	0.490	/
Density [g/cm^3]	1.15	1.27	0.08	0.018

The nodes of the root cross-section have been totally constrained in order to simulate the clamping boundary condition coming from the connection with the fuselage. The loading condition corresponds to a straight-and-level flight. By using the XFOIL [25] and AVL [26] software packages, the aerodynamic loads distribution on the upper and lower panel has been obtained and then condensed as concentrated forces acting on the ribs (Figure 5). Figure 6 shows the static deformation of the half-wing.

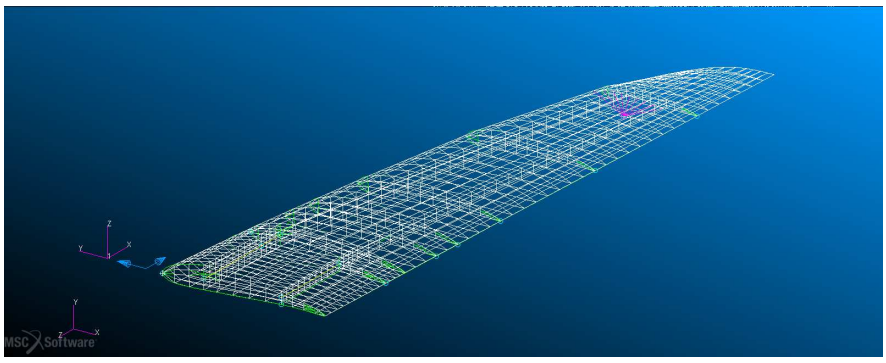

(**a**)

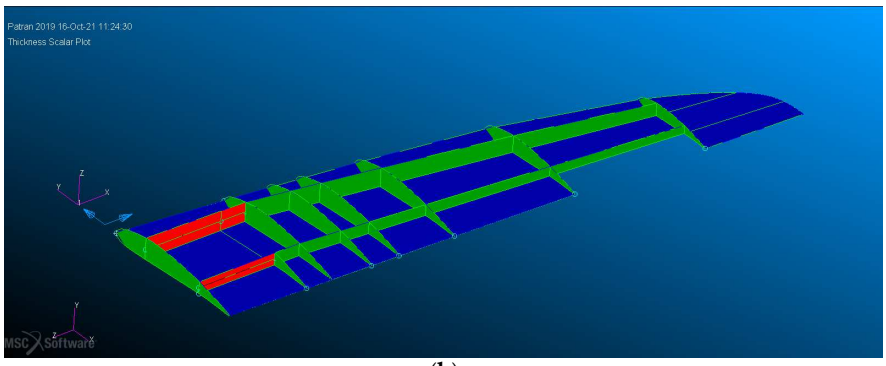

(**b**)

Figure 4. *Cont.*

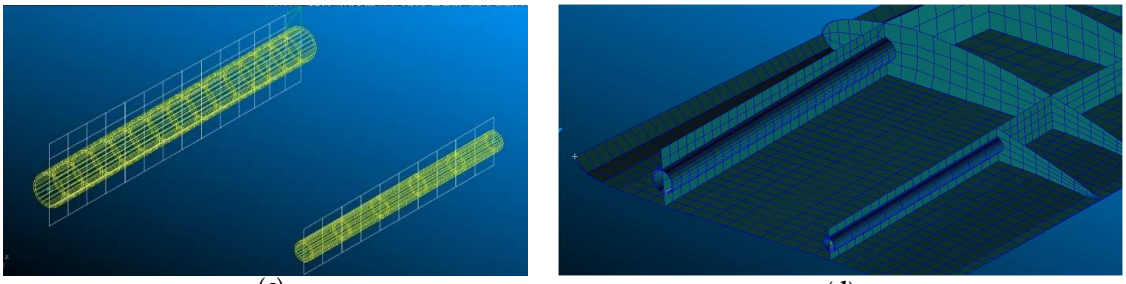

(**c**) (**d**)

Figure 4. Finite elements Half-wing model. (**a**) Half wing FE model, (**b**) Half-wing FE model with associated properties: Balsa (green) for ribs and spars, Foam + CFRP (red) for the tubular spars, GFRP (blue) for the upper and lower panels, (**c**) Tubular spars discretization: BAR2 elements (yellow) for the CFRP spars and QUAD4 elements (white) for the connection with the skin, (**d**) 3D visualization of tubular spars.

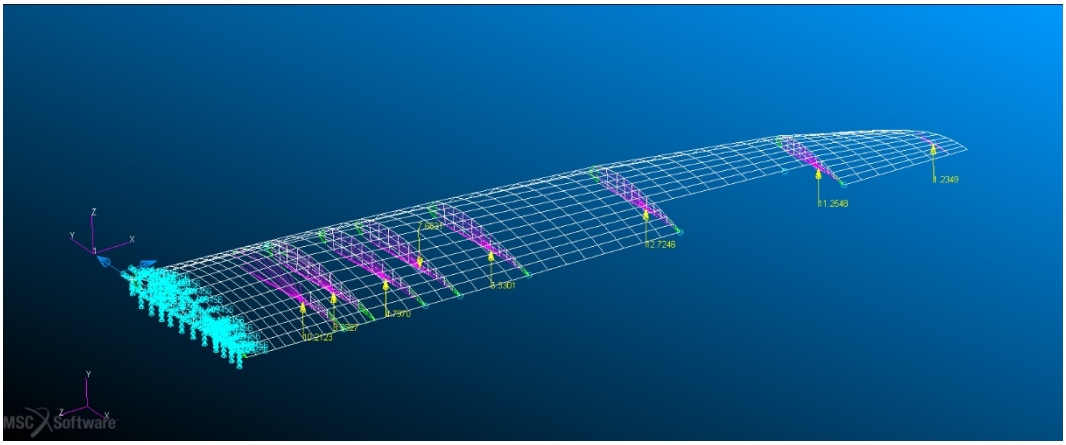

Figure 5. Half-wing boundary and loading conditions (concentrated forces have both y-axis and a z-axis component, then are applied to each rib by means of rigid connections and correspond to the aerodynamic loads experienced during a straight-and-level flight).

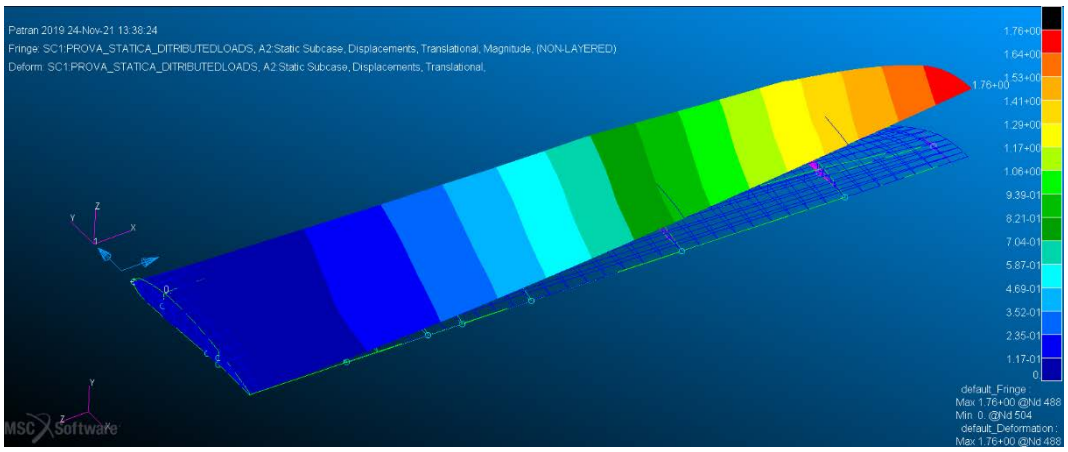

Figure 6. Half-wing deformed shape and displacements (magnitude) distribution (mm).

4. Results

4.1. Shape-Sensing Comparative Investigation

This section presents the results of the shape-sensing of the half-wing undergoing a static deformation under flight loads by using the Ko's Displacement Theory and the Modal Method.

Ko's Displacement Theory has been applied to the half-wing by considering two measurement lines along the span of the upper panel and by measuring the upper-panel external surface axial strain (ε_{ss}) at some locations (Figure 7). At each location, the strain has been evaluated from the FE model (when the location corresponds to the centroid of an element, the value is simply read from the results report whereas, when the location corresponds to a mesh node, the strain is averaged over the elements sharing that node, appropriate coordinate transformation has been applied in order to obtain the strain along each measuring line). Strains at the root were not read directly from the FE model at that location, but evaluated through an extrapolation procedure based on the three measurement locations close to the clamped end and on the same measurement line. The two lines have the same number of strain-measuring locations and are located at the same distances from the root cross-section in order to evaluate the twist rotation.

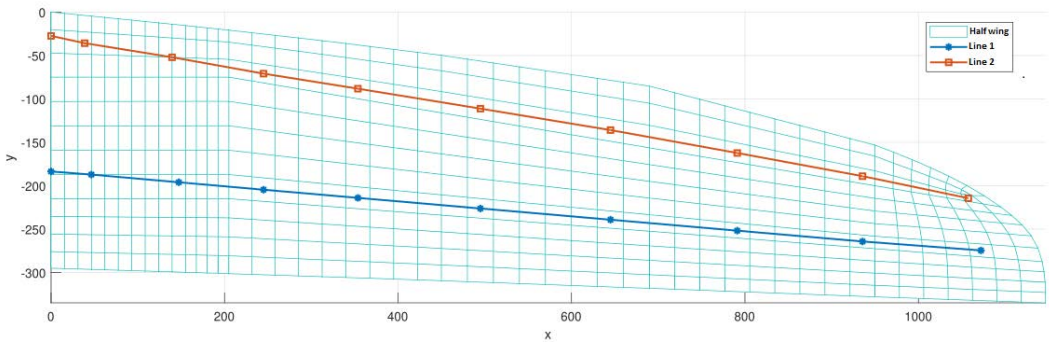

Figure 7. Half-wing with strain measuring lines on the upper panel for the application of the Ko's Displacement Theory.

Since the strain measurement locations are at different distances (c) from the neutral axis of the half-wing and since the neutral axis is different at different cross-sections along the span, a procedure is required to determine the position of the neutral axis at some key cross-sections [27]. According to the Bernoulli–Euler beam theory, the axial stress has a linear distribution over any cross-section

$$\sigma_{xx} = b_1 + b_2\, y + b_3\, z \tag{19}$$

If, for a given cross-section, three values of σ_{xx} are available, the coefficients b_1, b_2 and b_3 can be calculated and, by setting $\sigma_{xx} = 0$, the local neutral axis equation can be determined. Three cross-sections (at 0, 245, and 645 mm from the root rib, respectively) have been considered and the relative neutral axes have been determined. Between the root and the 2nd cross-section, the neutral axis has been considered to be the one determined for the root cross-section, similarly between the 2nd and 3rd cross-section. The neutral axis of the 3rd cross-section has been assumed to be valid until the wing-tip (Figure 8).

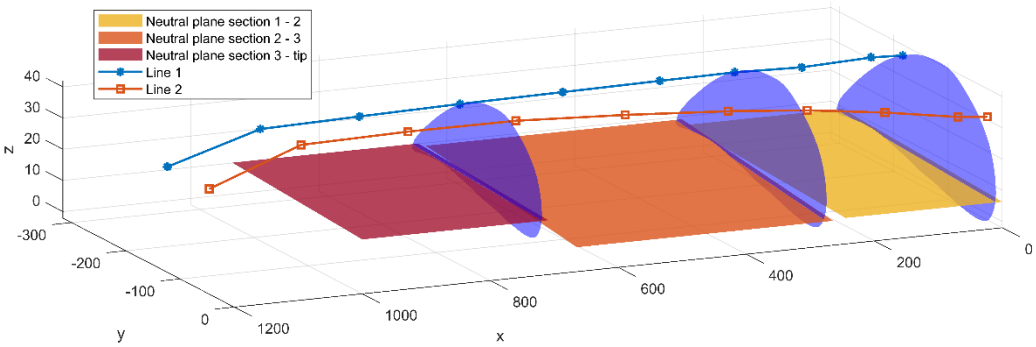

Figure 8. Neutral planes and measuring lines for Ko's Displacement Theory. Cross-sections considered for neutral axis calculation are represented in purple color.

For the application of the Modal Method, the selection of the mode shapes is performed according to the procedure described in Section 2.2. Figure 9 shows the energy carried by each mode (Equation (18)) as a percentage of the total strain energy associated with the static deformation of the half-wing. Almost all the energy is carried by the first mode shape since it is very similar to the static deformed shape, and three modes, carrying more than 99% of the total energy, are considered for the application of the Modal Method (Table 4): the first and the second mode shape and the residual vector (21st among the calculated modes), Figure 10.

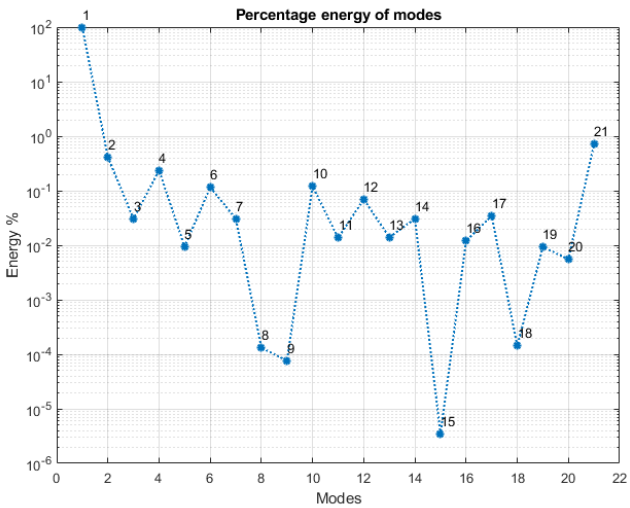

Figure 9. Percent strain energy of the first 20 mode shapes (and of the first residual vector, 21st among the calculated ones).

Table 4. Detail of the chosen mode shapes.

Total Strain Energy Associated with the Static Deformation [J]	**15.012**	
Mode Shape	**Strain energy [J]**	**Percent strain energy w.r.t. the total strain energy [%]**
1	14.7	98.1
2	0.0619	0.412
Residual vector	0.1068	0.712
Tot	14.9	99.27

The same locations and strain evaluation procedures already applied for the Ko's Displacement Theory have been adopted for the Modal Method.

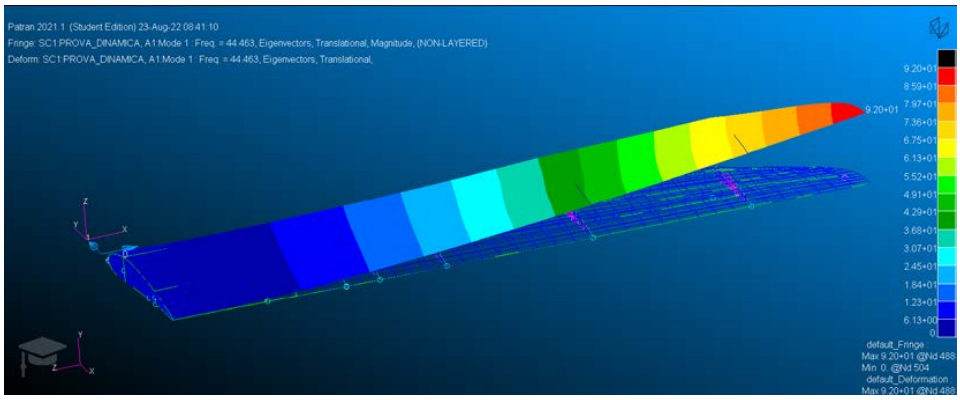

(**a**)

Figure 10. *Cont.*

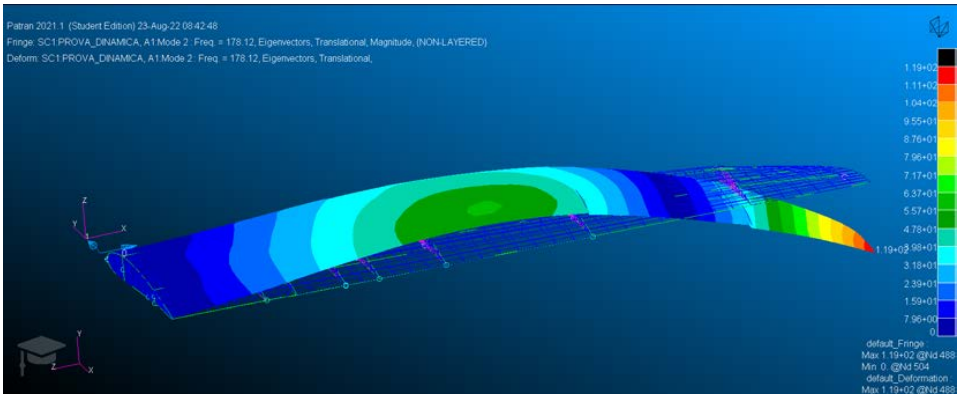

(**b**)

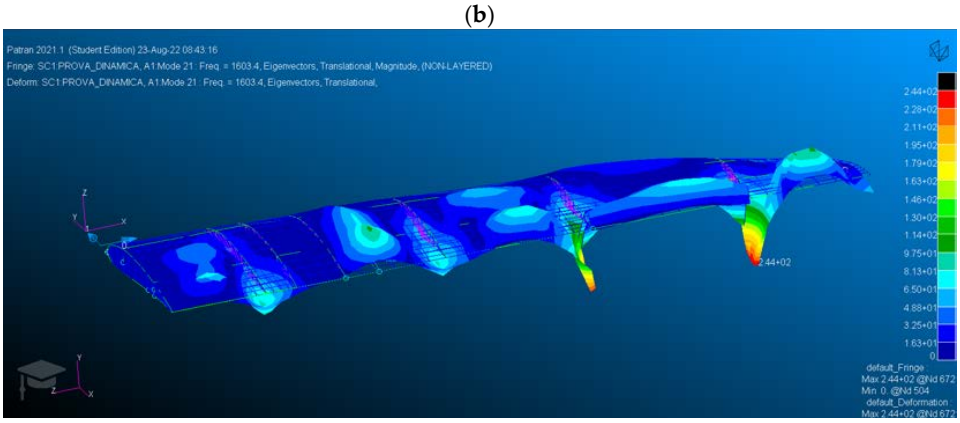

(**c**)

Figure 10. FEM modal analysis, deformed shape, and displacements (magnitude) distribution (mm): (**a**) first mode shape; (**b**) second mode shape; (**c**) residual vector.

The Ko's Displacement Theory and the Modal Method are compared in terms of accuracy of the reconstructed shape w.r.t. to the reference FEM static deformation, in particular using the following percent errors

$$\%ERMS_w = 100 \times \sqrt{\frac{1}{n}\sum_{i=1}^{n}\left(\frac{w_i - w_i^{ref}}{w_{max}^{ref}}\right)^2} \tag{20}$$

$$\%ERMS_\beta = 100 \times \sqrt{\frac{1}{n}\sum_{i=1}^{n}\left(\frac{\beta_i - \beta_i^{ref}}{\beta_{max}^{ref}}\right)^2} \tag{21}$$

In Equation (20), w_i is the deflection evaluated at the ith location by any of the two shape-sensing methods, w_i^{ref} is the corresponding reference deflection of the finite element model, w_{max}^{ref} is the maximum FEM deflection and n is the number of available reconstructed deflections. Since Ko's Displacement Theory is only able to evaluate deflections at the same locations where strains are known as input data on a specific measurement line, the error is evaluated per each sensing line and $n = 10$, whereas the Modal Method allows a full-field reconstruction of deflections, thus $n = 1500$, i.e., the whole set of nodes of the half-wing. A similar equation and similar definitions apply for the error related to the twist angle, Equation (21). In this case, $n = 10$ for both methods since the evaluation of the twist angle according to Equation (4) is performed on the 10 pairs of points along the wing-span belonging to the two sensing lines (Figure 7). Table 5 provides the $\%ERMS_w$ and $\%ERMS_\beta$ of the Ko's Displacement Theory and of the Modal Method, and Figure 11 shows the deflection and twist angle distribution along the wing span as calculated with the FE model and reconstructed by the shape-sensing approaches.

Table 5. Overall errors for Ko's Displacement Theory and Modal Method.

	Ko		MM	
	Line 1	Line 2	Mode shapes 1st and 2nd (residual vector omitted)	Mode shapes 1st, 2nd and residual vector
$\%ERMS_w$	11.07	10.31	1.434	1.334
$\%ERMS_\beta$	20.13		12.05	13.19

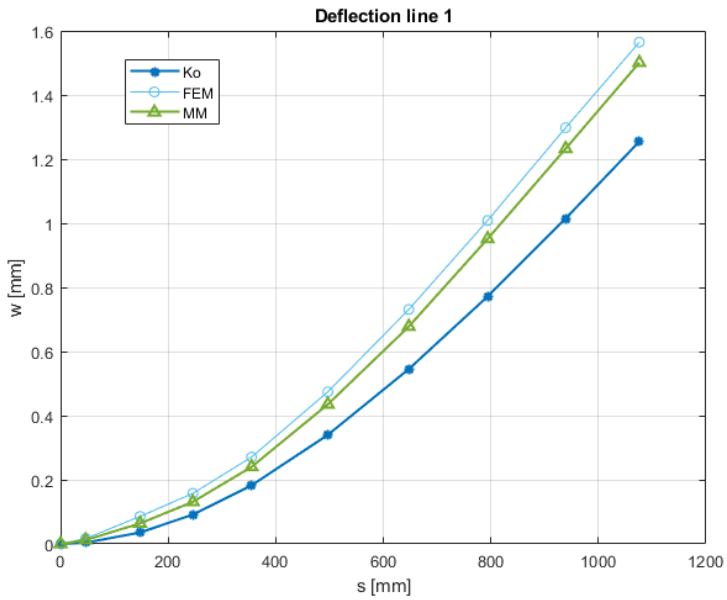

(**a**)

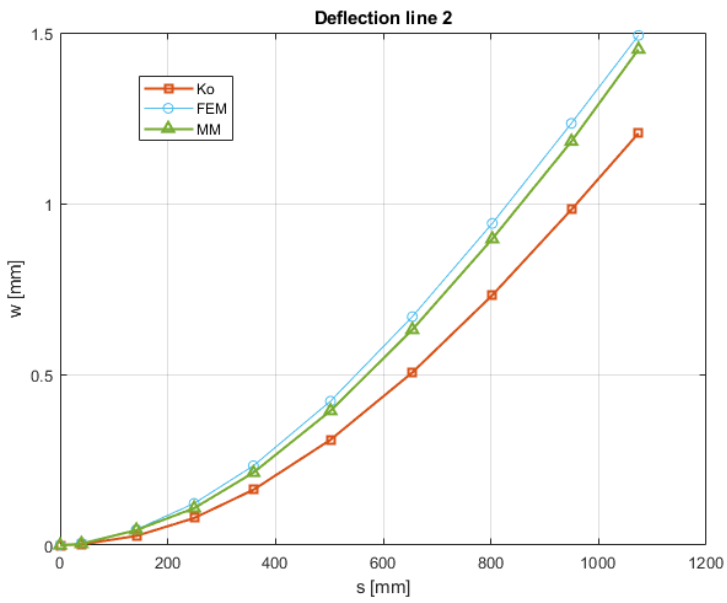

(**b**)

Figure 11. *Cont.*

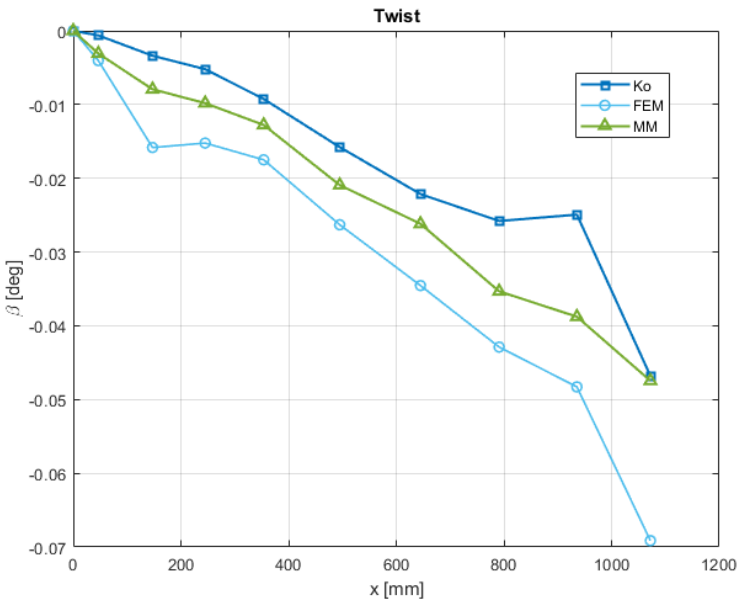

(**c**)

Figure 11. Result comparison between Modal Method (MM), Ko's Displacement Theory (Ko), and FEM static analysis (FEM): (**a**) deflection along the first sensing line; (**b**) deflection along the second sensing line; (**c**) twist computed through the lines deflection.

Results collected in Table 5 highlight the superior accuracy of the Modal Method compared with the performance of Ko's Displacement Theory. This is particularly true for the deflection, whereas the twist angle reconstruction generally leads to poorer results by using both shape-sensing approaches. The Ko's Displacement Theory seems to provide less accurate results as a consequence of some additional approximations (extrapolation to obtain the strain at the root of the sensing line, evaluation of the neutral axis at different cross-sections along the wing span). On the other hand, the Modal Method is devoid of similar approximations and is able to reconstruct the displacement field over the whole structural domain. The inclusion of the residual vector among the considered mode shapes slightly contributes to the reconstruction of the deflections (and has a small negative effect in terms of twist angle evaluation).

4.2. Enhancement of the Modal Method results

Since the Modal Method outperforms the Ko's Displacement Theory, it is worthwhile investigating further possible improvements.

An analysis on how the considered mode shapes affect the accuracy of the reconstructed deflection has been conducted. The number and location of strain measurement points are the same as in the previous comparison with Ko's Displacement Theory (Figure 7).

Table 6 reveals, at first, that those mode shapes that heavily contribute to describe the static deformation have to be included in the analysis (1st mode shape in the current case). On the other hand, simply adding mode shapes to increase the amount of strain energy representation w.r.t. the total strain energy does not always guarantee an increase of accuracy (using mode shapes 1:5 provides less accurate results w.r.t. using only the 1st mode shape even if the latter choice leads to a lower representation of the strain energy). In other words, the strain energy-based mode selection criterion can provide preliminary guidelines to detect fundamental modes, but additional mode shapes should be selected using different approaches.

Table 6. $\%ERMS_w$ errors for different sets of used mode shapes with the Modal Method (1:5 = from mode 1 to 5).

Used Mode Shapes	Percent Strain Energy Represented w.r.t. the Total Strain Energy [%]	$\%ERMS_w$
2:17	1.13	51.71
1	98.14	1.924
1:5	98.83	3.408
1:15	99.23	3.319
1, 2, 21	99.27	1.334
1:3, 21	99.30	1.450
1:5, 21	99.54	2.169

Moreover, by keeping the choice of mode shapes 1, 2, and the residual vector that provides the best results (Table 6), an optimization of the number and location of strain sensors is performed in order to assess the capability of the Modal Method to be accurate also with a reduced set of input strain data. A genetic algorithm has been used to minimize the $\%ERMS_w$ error. Each individual is represented by a set of 5 strain gauges, each located at the centroid of any of the finite elements of the upper panel external surface. For a given centroid/element, the available measurement directions are those of the in-plane element reference system. The genetic algorithm adopts a fitness-proportional ranking method and 1% mutation probability, 20 individuals are present in each generation, elitism strategy is included, and the stop criterion is based on either reaching a limit number of generations (100) or achieving $\%ERMS_w = 0.4$. The optimal sensors configuration and strain measurement directions ($\%ERMS_w = 0.38$) is based on 5 strain gauges, as shown in Figure 12. This excellent result, together with the reduced number of used strain gauges, further proves the efficiency of the Modal Method.

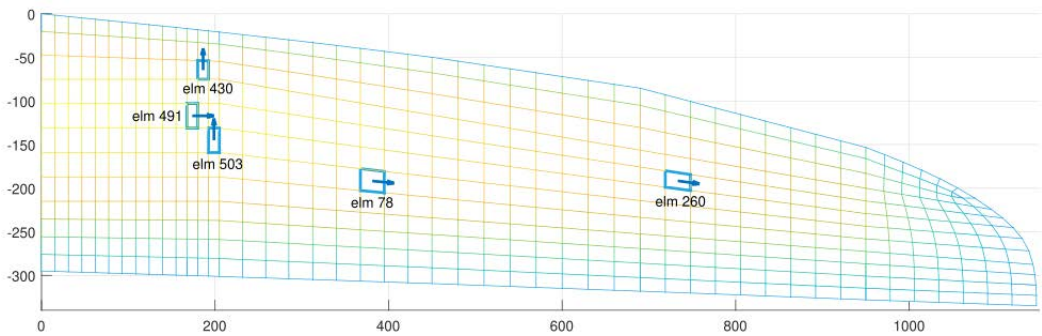

Figure 12. Optimal strain gauges configuration.

5. Conclusions

The paper presents a comparative study of two shape-sensing approaches, Ko's Displacement Theory and the Modal Method, applied to the deflection and twist-angle reconstruction of a multirotor UAV half-wing from discrete surface strain measurements. Both approaches are briefly presented and the UAV half-wing finite element model is described, which simulates the static response to straight-and-level flight conditions.

The deformed shape reconstructed by the Modal Method is globally very accurate, especially in terms of the deflection, whereas poorer results are found for the twist angle. Ko's Displacement Theory, with the same set of strain input data, is less accurate and this performance can be attributed to some further approximations that the approach inherently requires (extrapolation procedures to obtain the strain at the root cross-section, where it is expected to be practically impossible to set strain gauges, and the need to determine the location of the neutral axis along the wing span). The Modal Method can be further enhanced by investigating which mode shapes better contribute to the reconstruction of

the deflected shape, thus revealing that a criterion based on the static deformation strain energy contribution can provide important but only preliminary guidelines. Moreover, an optimization of the strain sensors' location is shown to be an efficient tool to reduce the number of required input strains to practically affordable values while keeping high levels of accuracy.

Further investigations, also experimental, are required to assess the accuracy and robustness of the Modal Method when different loading conditions and wing geometries have to be taken into account. Nevertheless, the Modal Method appears to be a very promising method for wing-structures shape-sensing in terms of accuracy and reduced number of required sensors.

Author Contributions: Conceptualization, M.G., M.E. and F.V.; methodology, M.G., M.E. and F.V.; software, F.V.; validation, M.E. and F.V.; formal analysis, F.V.; investigation, F.V.; resources, F.V.; data curation, F.V.; writing—original draft preparation, M.G., M.E. and F.V.; writing—review and editing, M.G., M.E. and F.V.; visualization, F.V.; supervision, M.G.; project administration, M.G.; All authors have read and agreed to the published version of the manuscript.

Funding: This research received no external funding.

Informed Consent Statement: Informed consent was obtained from all subjects involved in the study.

Data Availability Statement: Not applicable.

Acknowledgments: The authors gratefully acknowledge Daniele Camatti (PROS3) for providing data on the ICON V2 multirotor UAV.

Conflicts of Interest: The authors declare no conflict of interest.

References

1. Gherlone, M.; Cerracchio, P.; Mattone, M. Shape sensing methods: Review and experimental comparison on a wing-shaped plate. *Prog. Aerosp. Sci.* **2018**, *99*, 14–26. [CrossRef]
2. Evenblij, R.; Kong, F.; Koimtzoglou, C.; Ciminello, M.; Dimino, I. Shape sensing for morphing structures using fiber Bragg grating technology. In *Smart Intelligent Aircraft Structures (SARISTU)*; Springer: Cham, Switzerland, 2016; pp. 471–491.
3. Brian, J.S.; Dawn, K.G.; Wolfe, M.S.; Mark, E.F. High resolution optical frequency domain reflectometry for characterization of components and assemblies. *Opt. Express* **2005**, *13*, 666–674.
4. Di Sante, R. Fibre Optic Sensors for Structural Health Monitoring of Aircraft Composite Structures: Recent Advances and Applications. *Sensors* **2015**, *15*, 18666–18713. [CrossRef] [PubMed]
5. Ko, W.L.; Tran, V.T.; Richards, W.L. *Displacement Theories for In-Flight Deformed Shape Predictions of Aerospace Structures*; National Aeronautics and Space Administration, Dryden Flight Research Center: Edwards, CA, USA, 2007.
6. Akl, W.; Poh, S.; Baz, A. Wireless and distributed sensing of the shape of morphing structures. *Sens. Actuators A Phys.* **2007**, *140*, 94–102. [CrossRef]
7. Bogert, P.; Haugse, E.; Gehrki, R. Structural shape identification from experimental strains using a modal transformation technique. In Proceedings of the 44th AIAA/ASME/ASCE/AHS/ASC Structures, Structural Dynamics, and Materials Conference, Norfolk, VA, USA, 7–10 April 2003.
8. Foss, G.; Haugse, E. Using modal test results to develop strain to displacement transformations. In Proceedings of the 13th International Modal Analysis Conference, Nashville TN, USA, 13–16 February 1995.
9. Tessler, A.; Spangler, J.L.; Gherlone, M.; Mattone, M.; Di Sciuva, M. *Real-Time Characterization of Aerospace Structures Using Onboard Strain Measurement Technologies and Inverse Finite Element Method*; National Aeronautics and Space Administration Hampton Va Langley Research Center: Hampton, VA, USA, 2011.
10. Tessler, A.; Spangler, J.L. An inverse FEM for application to structural health monitoring. In Proceedings of the 14th US National Congress of Theoretical and Applied Mechanics, Blacksburg, VA, USA, 23–28 June 2002.
11. Tessler, A.; Spangler, J.L. A least-squares variational method for full-field reconstruction of elastic deformations in shear-deformable plates and shells. *Comput. Methods Appl. Mech. Eng.* **2005**, *194*, 327–339. [CrossRef]
12. Bruno, R.; Toomarian, N.; Salama, M. Shape estimation from incomplete measurements: A neural-net approach. *Smart Mater. Struct.* **1994**, *3*, 92–97. [CrossRef]
13. Mao, Z.; Todd, M. Comparison of shape reconstruction strategies in a complex flexible structure. In *Sensors and Smart Structures Technologies for Civil, Mechanical, and Aerospace Systems*; SPIE: Bellingham, WA, USA, 2008.
14. Esposito, M.; Gherlone, M. Composite wing box deformed-shape reconstruction based on measured strains: Optimization and comparison of existing approaches. *Aerosp. Sci. Technol.* **2020**, *99*, 105758. [CrossRef]

15. Esposito, M.; Gherlone, M. Material and strain sensing uncertainties quantification for the shape sensing of a composite wing box. *Mech. Syst. Signal Process.* **2021**, *160*, 107875. [CrossRef]
16. Ko, W.L.; Richards, W.L.; Fleischer, V.T. *Applications of Ko Displacement Theory to the Deformed Shape Predictions of the Doubly-Tapered Ikhana Wing*; NASA Dryden Flight Research Center: Edwards, CA, USA, 2009.
17. Jutte, C.V.; Ko, W.L.; Stephens, C.A.; Bakalyar, J.A.; Richards, W.L. *Deformed Shape Calculation of a Full-Scale Wing Using Fiber Optic Strain Data from a Ground Loads Test*; National Aeronautics and Space Administration, Dryden Flight Research Center: Edwards, CA, USA, 2011.
18. Pisoni, A.; Santolini, C.; Hauf, D.; Dubowsky, S. Displacements in a vibrating body by strain gage measurements. In *Proceedings-SPIE the International Society for Optical Engineering*; Society of Photo-Optical Instrumentation Engineers: Bellingham, WA, USA, 1995.
19. Rapp, S.; Kang, L.H.; Han, J.H.; Mueller, U.C.; Baier, H. Displacement field estimation for a two-dimensional structure using fiber Bragg grating sensors. *Smart Mater. Struct.* **2009**, *18*, 025006. [CrossRef]
20. SIEMENS. *Basic Dynamic: Analysis User's Guide*; SIEMENS: Munich, Germany, 2014.
21. Rose, T. *Using Residual Vectors in MSC Nastran Dynamic Analysis to Improve Accuracy*; MacNeal-Schwendler Corp: Universal City, CA, USA, 1991.
22. Dickens, J.; Nakagawa, J.; Wittbrodt, M. A critique of mode acceleration and modal truncation augmentation methods for modal response analysis. *Comput. Struct.* **1997**, *62*, 985–998. [CrossRef]
23. Wijker, J. *Mechanical Vibrations in Spacecraft Design*; Springer: Berlin/Heidelberg, Germany, 2004; pp. 331–340.
24. Camatti, D. PROS3 Engineering & Robotics, PROS3. Available online: https://www.pros3.eu/ (accessed on 30 July 2022).
25. Drela, M.; Youngren, H. XFOIL, MIT. Available online: https://web.mit.edu/drela/Public/web/xfoil (accessed on 30 July 2022).
26. Drela, M.; Youngren, H. AVL, MIT. Available online: http://web.mit.edu/drela/Public/web/avl/ (accessed on 30 July 2022).
27. Ardillo, M.; Gherlone, M. Shape Sensing Della Semiala di un Prototipo da Competizione. BSc Thesis, Politecnico di Torino, Turin, Italy, 2018.